Efficient Planar Perovskite Solar Cells with Improved Fill Factor via Interface Engineering with Graphene

Xiaojuan Zhao,[†] Leiming Tao,[†] Hao Li,[†] Wenchao Huang,[‡] Pengyu Sun,[‡] Jun Liu,[§] Shuangshuang Liu,[†] Qiang Sun,[†] Zhifang Cui,[‖] Lijie Sun,[⊥] Yan Shen,[†] Yang Yang,[‡] and Mingkui Wang*,[†]

[†]Wuhan National Laboratory for Optoelectronics, School of Optical and Electronic Information, Huazhong University of Science and Technology, 1037 Luoyu Road, Wuhan 430074, P. R. China

[‡]Department of Materials Science and Engineering, University of California Los Angeles, 405 Hilgard Avenue, Los Angeles, California 90095-9000, United States

[§]State Key Laboratory of Polymer Physics and Chemistry, Changchun Institute of Applied Chemistry, Chinese Academy of Sciences, Changchun 130022, P. R. China

[‖]College of Chemical and Environmental Engineering, Shandong University of Science and Technology, Qingdao 266590, P. R. China

[⊥]State Key Laboratory of Space Power Technology, Shanghai Institute of Space Power Sources, Shanghai 200245, P. R. China

S *Supporting Information*

ABSTRACT: Organic–inorganic hybrid lead halide perovskites have been widely investigated in optoelectronics both experimentally and theoretically. The present work incorporates chemically modified graphene into nanocrystal SnO_2 as the electron transporting layer (ETL) for highly efficient planar perovskite solar cells. The modification of SnO_2 with highly conductive two-dimensional naphthalene diimide-graphene can increase surface hydrophobicity and form van der Waals interaction between the surfactant and the organic–inorganic hybrid lead halide perovskite compounds. As a result, highly efficient perovskite solar cells with power conversion efficiency of 20.2% can be achieved with an improved fill factor of 82%, which could be mainly attributed to the augmented charge extraction and transport.

KEYWORDS: *Electron transporting, perovskite solar cell, graphene, van der Waals interaction, interface engineering*
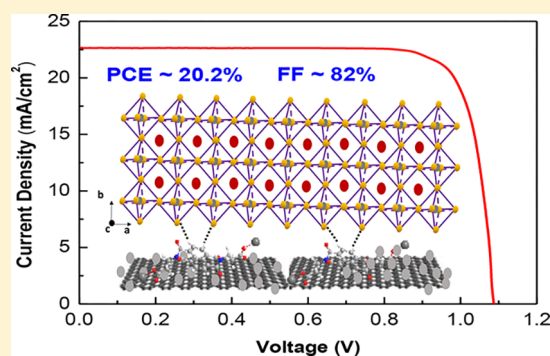
Because of the long carrier diffusion length (>1 μm), high charge mobility (~0.6 cm^2 V^{-1} s^{-1}), high absorption coefficient (5.7 × 10^4 cm^{-1} at 600 nm), and ordinary fabrication processes, organic–inorganic hybrid lead halide perovskite solar cells (PSCs) have received great attention for the ability of converting sunlight directly into electrical power. The power conversion efficiency (PCE) of PSCs has rapidly increased above 22% in a short period, rendering the efficiency comparable with current commercial technologies.[1] Organic–inorganic hybrid lead perovskite exhibits a general formula of ABX_3, where A represents $CH_3NH_3^+$ (MA), $HC(NH_2)_2^+$ (FA), or Cs^+; B represents Pb^{2+} or Sn^{2+}; and X represents halogen ions Cl^-, Br^-, or I^-. Although $MAPbI_3$ has been widely used as the active layer in PSCs, it has shown numerous disadvantages such as instable crystal phase under humidity and solvents. Cesium-containing $Cs_{0.2}FA_{0.8}PbI_{2.84}Br_{0.16}$ material absorber was reported with a PCE of 17.35% with features of high stability and reproducibility.[2,3] In addition, interface engineering has become an effective strategy to tune the optoelectronic properties and thus improve device performance.[4–7]

The Shockley–Queisser efficiency limit has pointed out that the fill factor (FF) for efficient single junction devices can reach as high as ~90% at room temperature.[8,9] However, most of the reported FF values for planar PSCs are in the range 60–70%,[10] indicating that further improving FF can become one of the effective strategies to enhance device efficiency. For example, a small amount of H_2O was added into PbI_2/dimethylformamide (DMF) precursor solution to achieve a remarkable FF of 85%, giving a high PCE of 18% compared to the controlled one (15%),[9] which was because of the highly pure perovskite film fabricated from the high-quality PbI_2 film after a small amount of H_2O was added into PbI_2/DMF precursor solution. One of the possible reasons to explain a low FF can be related to the loss mechanism originated from inefficient charge extraction of cells. Different attempts have been made to increase device FFs by inducing crystal lattice orientation of perovskite,[11] as well as controlling interfacial microstructures.[12,13] Among these successful methods, the passivation of grain boundaries[14–16] and the nonstoichiometric precursor solution with excess PbI_2 have turned out to be remarkable.[17,18] So far, Lewis-base
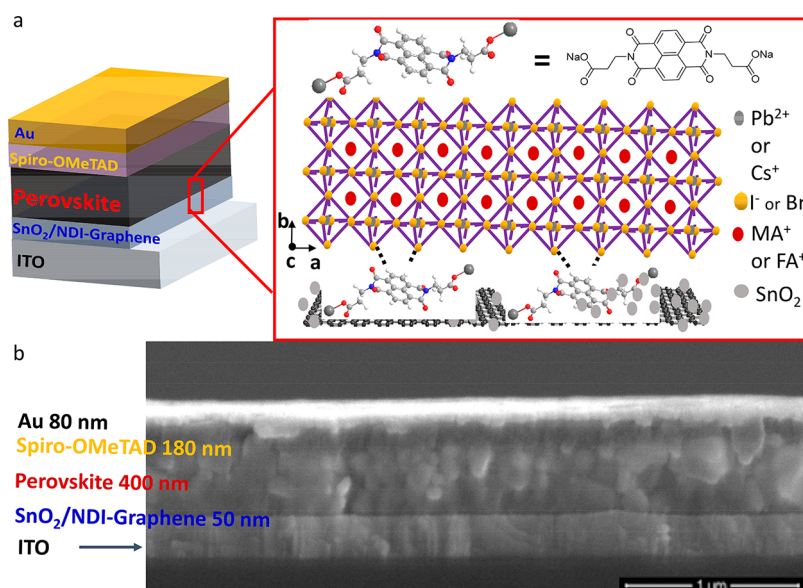
Figure 1. (a) Schematic architecture of planar perovskite solar cells. The expanded scheme shows the chemical structure of NDI and the bonding condition of NDI-graphene with perovskite films. (b) Cross-sectional SEM image of $FA_{0.75}MA_{0.15}Cs_{0.1}PbI_{2.65}Br_{0.35}$ deposited on SnO_2-5% G substrates by one-step spin-coating method.
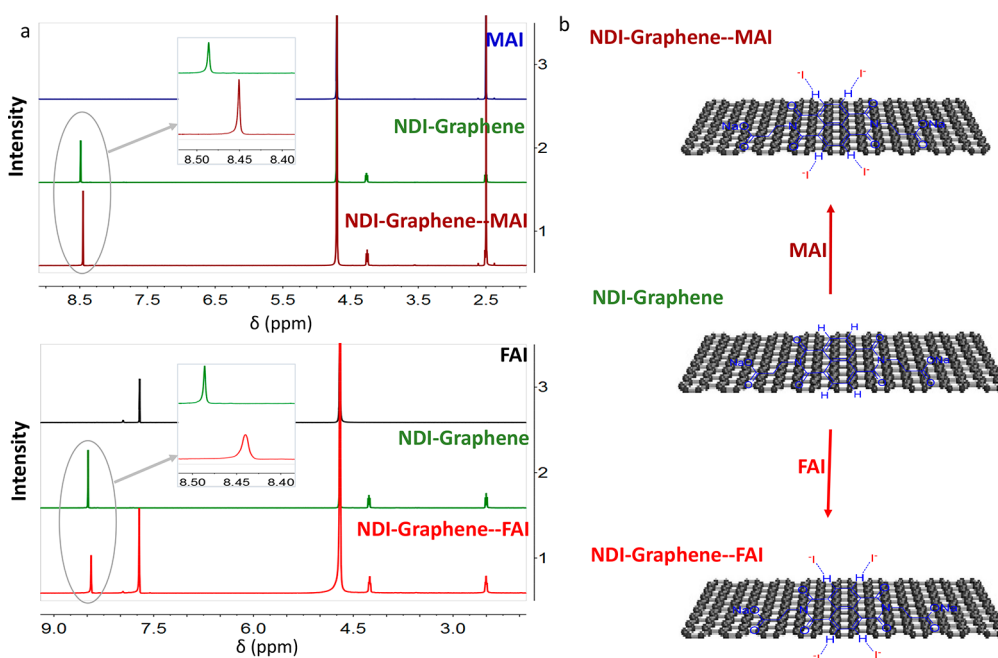

Figure 2. (a) Corresponding ^1H NMR spectra showing changes in the resonance signals arising from the H protons of NDI-graphene on addition of MAI or FAI solution in deuterated water at 298 K. (b) Representation of the supramolecular weak van der Waals interaction in the MAI- or FAI-containing NDI-graphene.

passivation and fullerene passivation have been demonstrated to be able to improve device FF values and thus solar cell efficiency. The PbI_2 (Lewis acid) tends to form adducts via interacting with polar aprotic solvents (Lewis base)[19] containing sulfur, oxygen, or nitrogen, such as dimethyl sulfoxide (DMSO),[20−23] DMF,[24] and N-methyl-pyrrolidone.[25] After solvent evaporation, the retained PbI_2 may locate within the grain boundaries of the perovskite crystal film or at the interface between perovskite and interlayer. For example, an excess PbI_2 induced at the active perovskite/TiO_2 interface could facilitate electron injection into the TiO_2 layer, resulting in an enhanced FF of 76%.[26,27] Furthermore, several nano-

composites, such as graphene quantum dots/SnO_2,[28] graphene/TiO_2,[29] ZnO nanorod arrays,[30] perovskite oxide $SrTiO_3$,[31] and SnO_2 nanocrystals,[32] were reported as electron transporting layers (ETLs) for PSCs to enhance the devices' performances. However, the obtained values of FF (~76%) are still lower than the expectation. Though different strategies to improve FF mainly depend on the passivation and optimization of perovskite absorbers, it is noticed that little information about modification of ETLs has been reported. To further booster the FF > 80%, herein we report a new nanocomposite for a highly efficient PSC via interfacial engineering by using two-dimensional electronic conducting graphene modified with
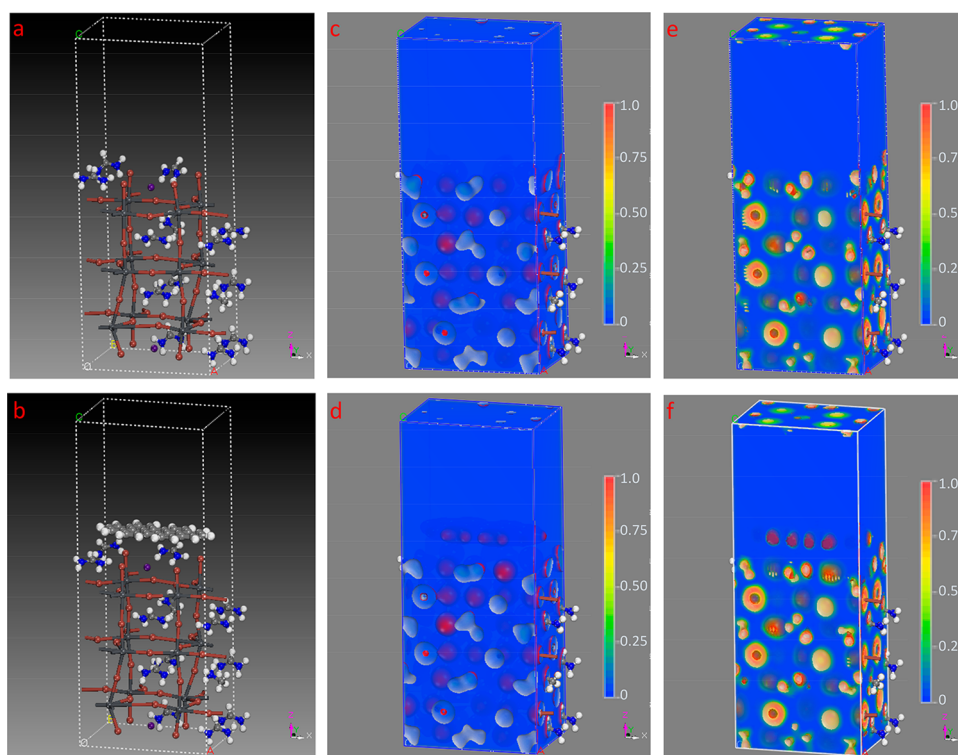
Figure 3. (a) Atomic configuration of $FA_{0.75}MA_{0.15}Cs_{0.1}PbI_{2.65}Br_{0.35}$ (the light gray atom is C, the white atom is H, the dark gray atom is Pb, the dark red atom is I, the blue atom is N, and the black atom is Cs). (b) Atomic configuration of $FA_{0.75}MA_{0.15}Cs_{0.1}PbI_{2.65}Br_{0.35}$/graphene (the light gray atom is C, the white atom is H, the dark gray atom is Pb, the dark red atom is I, the blue atom is N, and the black atom is Cs). (c) Distribution of electron density of $FA_{0.75}MA_{0.15}Cs_{0.1}PbI_{2.65}Br_{0.35}$. (d) Distribution of electron density of $FA_{0.75}MA_{0.15}Cs_{0.1}PbI_{2.65}Br_{0.35}$/graphene. (e) Electron localization function (ELF) of electrons at the $FA_{0.75}MA_{0.15}Cs_{0.1}PbI_{2.65}Br_{0.35}$ interface. (f) ELF of electrons at the $FA_{0.75}MA_{0.15}Cs_{0.1}PbI_{2.65}Br_{0.35}$/graphene interface.

the easily synthesized and planar N,N'-bis-[2-(ethanoic acid sodium)]-1,4,5,8-naphthalene diimide (NDI) surfactant. NDI can greatly improve the dispersion ability of exfoliated graphene in aqueous solution and tune the electronic energy levels of graphene.[33] The hydrogen atom of the benzene ring within the NDI can be capable of interacting with the iodine of perovskite crystals at the adjacent interface between the perovskite and ETL via van der Waals interaction. Thereby, the octahedral $[PbI_6]^{4-}$ can be controllably fixed to the perovskite/ETL interface, which has the same effect as the Lewis-base passivation effect.[26] As a result, rapid charge extraction and transport can be simultaneously obtained in the compact NDI-graphene-doped SnO_2 ETL-based PSC with an improved FF of 82%.

In this study, the SnO_2 ETL was prepared by spin-coating precursor solutions of 0.1 M $SnCl_2·2H_2O$ with/without NDI modified graphene in ethanol on a precleaned indium tin oxide (ITO) substrate,[33] followed by thermal annealing in the air at 150 °C for 30 min and at 180 °C for 60 min. We have previously reported a novel strategy to greatly improve the dispersion ability of graphene in aqueous solution.[34] Considering the high cost, high boiling point, and high environmental pollution characteristics of organic solvents, graphite exfoliation in an aqueous solution with surfactant is more suitable for mass production of graphene.[35] Indeed an aqueous solution is favorable to evaporate in a low-temperature-processed SnO_2 layer without any residue.

Figure 1a presents the schematic device architecture for a planar solar cell. Cross-sectional scanning electron microscope (SEM) images in Figure 1b were collected to show that the

thickness of the ETL is about 50 nm, 400 nm for the perovskite layer, 180 nm for the spiro-OMeTAD layer, and 80 nm for the Au electrode. Additionally, Figure 1a illustrates the possible van der Waals interaction between a hydrogen atom on the benzene ring of NDI of the ETL and an iodine atom of octahedral $[PbI_6]^{4-}$ of perovskite compounds. The interaction among NDI-graphene and mixed-cation lead hybrid perovskite compounds was characterized by performing liquid-state nuclear magnetic resonance spectroscopy (NMR) characterization of MAI, FAI, NDI-graphene, and their mixture. Figure 2a compares the ^1H NMR of pure MAI or FAI in deuterated water to assign the signal of van der Waals interaction for NDI-graphene···MAI and NDI-graphene···FAI. In the case of NDI-graphene···MAI, the proton signal of the NDI-graphene at δ = 8.49 ppm apparently moves toward the lower value of 8.45 ppm, while in the case of NDI-graphene···FAI, the proton signal at δ = 8.49 ppm moves to a lower δ = 8.44 ppm. The signal for the NDI group protons shifts upfield upon addition of MAI or FAI, which can be clearly rationalized in terms of a shielding effect of the N−H···I⁻ van der Waals interaction. This in turn supports our argument that the octahedral $[PbI_6]^{4-}$ can be anchored on top of the ETL. Figure 2b further illustrates the supramolecular van der Waals interaction among MAI or FAI with NDI-graphene. After the addition of MAI or FAI, the N−H···I⁻ van der Waals interaction forms between NDI-graphene and MAI or FAI. Density functional theory (DFT) calculations on the electronic structure at the perovskite/ETL interface were carried out to explore the impact of graphene. Figure 3a,b presents the geometry for the configuration of the optimized structures for perovskite and perovskite/graphene, respectively.
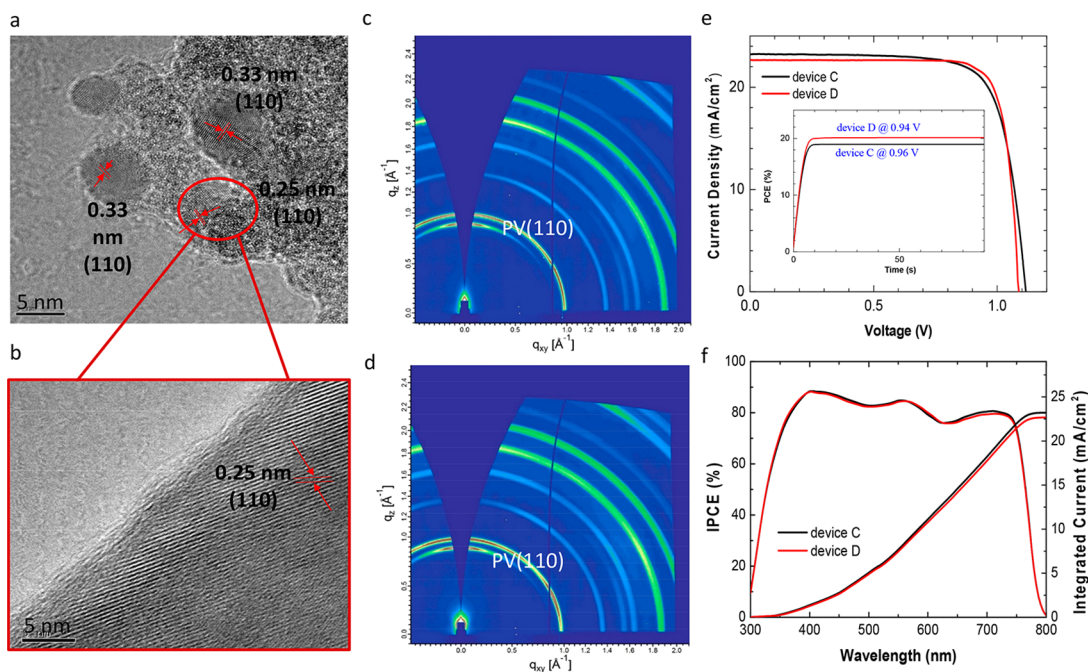
Figure 4. (a) FTEM image of the SnO_2 blend with NDI-graphene. (b) Zoomed-in FTEM image of the NDI-graphene region of blend films (red circle in part a). Two-dimensional GIWAXS patterns of (c) $FA_{0.75}MA_{0.15}Cs_{0.1}PbI_{2.65}Br_{0.35}$ film on ITO/SnO_2 and (d) $FA_{0.75}MA_{0.15}Cs_{0.1}PbI_{2.65}Br_{0.35}$ film on ITO/NDI-graphene substrates. (e) $J-V$ curves (reverse scan) of devices C and D based on SnO_2 and SnO_2-5% G ETL, respectively; inset is the maximal steady-state power output at the maximum power point for device C at 0.92 V, and device D at 0.94 V. (f) EQE spectra of corresponding devices.

Figure 3c,d shows the calculated electron density (ED) in the region of perovskite and perovskite/graphene, respectively. After interface engineering with graphene, the electrons of perovskite are dragged upward to the graphene, suggesting the existence of interaction. Furthermore, the interaction property was evaluated with the electron localization function (ELF). The values for the ELF profile in Figure 3e,f of ELF are in the range 0−1 with 0.5 (green) corresponding to a delocalized (metallic) electron gas and 1 (red) meaning complete localization. High ELF values are found at the interface of graphene and perovskite.[36] A reduced electron distribution in the interior perovskite region was found in the perovskite-graphene configuration, revealing the potential interaction.

We first investigated the optical and photophysical properties of SnO_2 films with different contents of NDI-graphene to determine their suitability as ETLs in PSCs. Figure S1 compares the transmission spectra of pristine SnO_2 film and SnO_2 with different-content NDI-graphene films (SnO_2-1% G represents SnO_2 with 1% v/v NDI-graphene; SnO_2-5% G, SnO_2 with 5% v/v NDI-graphene; and SnO_2-10% G, SnO_2 with 10% v/v NDI-graphene) on ITO substrates. These films exhibit high transmittance of about 90% in the visible range 400−800 nm. This makes these films favorable for utilization as ETLs to guarantee most photon flux reaching the perovskite absorber layer for generating photocurrent. The lattice spacing for the in-plane (110) and (110) facets of few-layered NDI-graphene and SnO_2 can be determined to be 0.25 and 0.33 nm with field-emission transmission electron microscopy (FE-TEM) in Figure 4a,b. The NDI-graphene has been successfully introduced into the SnO_2 network.[7,37,38] Further contact-angle measurements were carried out with water on ITO substrates with SnO_2 layers and different-content NDI-graphene-modified SnO_2 layers. We found that the contact angle of SnO_2 with NDI-graphene ETL increased from 66° to

92° as the NDI-graphene concentration changed from 0% to 10% (v/v) (Figure S2) because of the hydrophobicity of NDI-graphene.[39] Atomic force microscopy (AFM) characterization was further carried out to study the morphology of NDI-graphene-doped SnO_2 nanocrystal films and the perovskite films deposited on top of these ETLs (Figure S3). The root-mean-square (RMS) roughness for the substrate with 5 vol % NDI-graphene (RMS = 1.05 nm) shows the smallest value among those containing NDI-graphene. However, it is still two times higher than that of the case without NDI-graphene (RMS = 0.55 nm). The $FA_{0.75}MA_{0.15}Cs_{0.1}PbI_{2.65}Br_{0.35}$ films on corresponding ETLs follow the same tendency of RMS (Figure S4). The SEM images of $FA_{0.75}MA_{0.15}Cs_{0.1}PbI_{2.65}Br_{0.35}$ films on pristine SnO_2 and SnO_2-5% G substrates further confirm the negligible difference after adding NDI-graphene (Figure S5). Grazing incidence wide-angle scattering spectrum (GIWAXS) has also been used to clarify the effect of substrates on perovskite compound crystallization, as shown in Figure 4c,d. A strong scattering pattern located at q = 1 Å^{-1} corresponds to the (110) plane of perovskite.[40] From two-dimensional scattering patterns, the scattering intensity and orientation of the (110) peak on different substrates has a negligible difference. In addition, the X-ray diffraction of $FA_{0.75}MA_{0.15}Cs_{0.1}PbI_{2.65}Br_{0.35}$ films on pristine SnO_2 and SnO_2-5% G substrates showed the similar crystallization properties (Figure S7). These further demonstrate an ignorable influence of addition of NDI-graphene into SnO_2 substrates on the crystallization behavior of $FA_{0.75}MA_{0.15}Cs_{0.1}PbI_{2.65}Br_{0.35}$ films. A uniform surface of ETL is highly necessary for efficient PSCs to bring up high electron extraction. Figure S6 compares the UV−vis absorption spectra of the $FA_{0.83}MA_{0.17}PbI_{2.63}Br_{0.37}$ and $FA_{0.75}MA_{0.15}Cs_{0.1}PbI_{2.65}Br_{0.35}$ layers on NDI-graphene-doped SnO_2 and pristine SnO_2 substrates. We found that the perovskite absorber with Cs component showed slightly

Table 1. Device Parameters[a] (Reverse-Scan Data) of the $FA_{0.75}MA_{0.15}Cs_{0.1}PbI_{2.65}Br_{0.35}$ Solar Cells with SnO_2 (Device C) or SnO_2-5% G (Device D) under Illumination of AM 1.5 G, 100 mW cm^2

$FA_{0.75}MA_{0.15}Cs_{0.1}PbI_{2.65}Br_{0.35}$	V_{oc} [mV]	J_{sc} [mA cm^{-2}]	FF [%]	PCE [%]	R_s [Ω cm^2]	n	R_{sh} [kΩ cm^2]
device C (best)	1097	23.21	74.6	18.99	6.08	1.98	12.50
average	1091 ± 162	22.81 ± 0.73	73.85 ± 2.11	17.21 ± 2.37			
device D (best)	1084	22.66	82.1	20.16	1.51	1.95	1.22
average	1076 ± 197	21.81 ± 1.95	80.25 ± 1.93	18.83 ± 1.33			

[a]Note: average photovoltaic performance parameters including the standard errors of the J_{sc}, V_{oc}, FF, and PCE. The statistics are based on 10−20 cells on different substrates. The shunt resistance (R_{sh}) was calculated from the inverse of the slope of the J−V curves at 0 V.
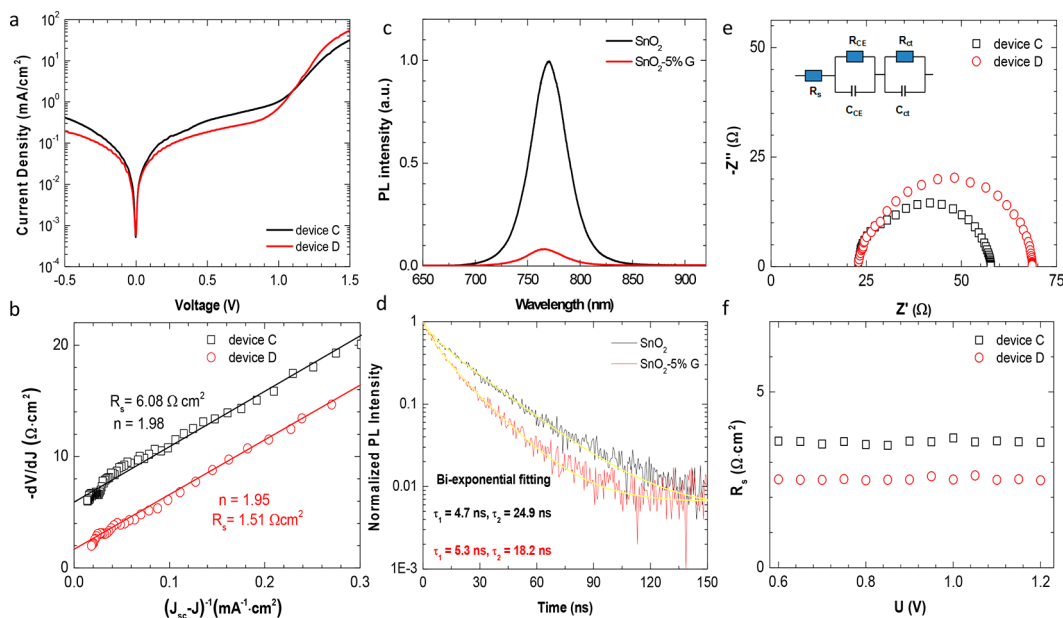

Figure 5. (a) J−V curves of devices C and D in the dark. (b) Plots of −dV/dJ vs (J_{sc} − J) − 1 and the linear fitting curves. (c) PL spectra of ITO/$FA_{0.75}MA_{0.15}Cs_{0.1}PbI_{2.65}Br_{0.35}$/$SnO_2$ and ITO/$FA_{0.75}MA_{0.15}Cs_{0.1}PbI_{2.65}Br_{0.35}$/$SnO_2$-5% G films on slide substrates. (d) TRPL decay spectra of $FA_{0.75}MA_{0.15}Cs_{0.1}PbI_{2.65}Br_{0.35}$ films with different ETL substrates. The fluency for the TRPL measurement at 770 nm is around 11 nJ cm^{-2}, and the excitation density is around 10^{14} cm^{-3}. The yellow line represents the fitted curve using the double exponential function. Electronic impedance spectroscopy measurements: (e) Nyquist plots obtained under illumination at a bias of 1.0 V for devices C and D. The inset shows the equivalent circuit for fitting the impedance spectroscopy data. (f) R_s as a function of the bias.

enhanced absorption between 400 and 750 nm, and exhibited a blue-shifted absorption edge from 783 nm in $FA_{0.83}MA_{0.17}PbI_{2.63}Br_{0.37}$ film (with an optical bandgap of 1.58 eV) to 779 nm (with higher optical band gap of 1.59 eV). Moreover, a blue-shifted absorption was also observed in the photoluminescence (PL) spectra (Figure S8) when the inorganic Cs component is added into the $FA_{0.75}MA_{0.15}Cs_{0.1}PbI_{2.65}Br_{0.35}$ compounds, which indicates passivated traps at the perovskite surface.[41] As reported, introducing graphene into the TiO_2 ETL in PSC devices effectively improves photovoltaic performance of PSCs; thus, the suitability of graphene for the ETL has been proven.[42] The band alignment of different ETLs was estimated to be −4.20, −4.27, −4.27, and −4.37 eV for SnO_2, SnO_2-1% G, SnO_2-5% G, and SnO_2-10% G, respectively, with the help from ultraviolet photoelectron spectroscopy (UPS) and transmission measurements in Figure S9a. The down-shifting conduction band of doped SnO_2 was probably derived from the low-lying conduction band of NDI-graphene. The conduction band of $FA_{0.75}MA_{0.15}Cs_{0.1}PbI_{2.65}Br_{0.35}$ was estimated to be −4.05 eV, which promotes efficient electron transport to ETLs (see Figure S9b). We measured space-charge-limited current (SCLC) of SnO_2-G films by using electron-only devices (Figure S10). A bigger current density for the SnO_2-5% G

device as compared to that of SnO_2 confirms its higher electrical conductivity.[43,44] The electron mobility of the ETL films can be obtained by fitting J−V curves using eq 1:

$$J = \frac{9}{8}\varepsilon_0\varepsilon_r\mu\frac{V^2}{d^3} \tag{1}$$

where J is the current density, μ is the zero-field mobility of electrons, ε_0 is the permittivity of the vacuum, ε_r is the relative permittivity of SnO_2 (=13), L is the thickness of the ETLs (50 nm), and V is the applied effective voltage. In these devices, the electron mobility can be determined because of the n-type property of SnO_2. The SnO_2-5% G ETL exhibits higher electron mobility (4.67 × 10^{-4} cm^2 V^{-1} s^{-1}), which is significantly higher than those of pure SnO_2 (9.11 × 10^{-5} cm^2 V^{-1} s^{-1}) and SnO_2-5% NDI (9.08 × 10^{-5} cm^2 V^{-1} s^{-1}). We concluded that the increase of electron mobility was derived from the highly electronic conductivity of graphene. Fast electron transporting would benefit from higher electron mobility.

Some preliminary photovoltaic experiments were conducted to evaluate the performance of the transparent SnO_2 ETL modified with NDI-graphene. Figure 4e presents the reverse-scan photocurrent density−voltage (J−V) characteristics of various devices. The detailed photovoltaic parameters such as

open-circuit voltage (V_{oc}), FF, short-circuit current density (J_{sc}), and PCE for devices are given in Table 1 and Table S1. The transparent NDI-graphene thin films (with the thickness of ~30 nm) were first tested as the ETL in planar device A with an architecture of ETL/FA$_{0.83}$MA$_{0.17}$PbI$_{2.63}$Br$_{0.37}$/spiro-OMe-TAD/Au. The J_{sc}, V_{oc}, and FF values of device A are 18.58 mA cm^{-2}, 1067 mV, and 49%, respectively, which yield an overall PCE of 9.8% (Table S1). Replacing the NDI-graphene with the SnO$_2$ ETL in device B can largely increase the PCE to 15.2%, especially with the FF rising to 63%. Device A shows lower V_{oc} than device B because of increased dark current. The device efficiency can be further increased by changing the light absorber to FA$_{0.75}$MA$_{0.15}$Cs$_{0.1}$PbI$_{2.65}$Br$_{0.35}$ (with the same ETL of SnO$_2$) in device C (Figure 4e, black curve) resulting in an 18.99% overall PCE with a J_{sc} of 23.21 mA cm^{-2}, a V_{oc} of 1097 mV, and a FF of 75% (Table 1). Impressively, adding NDI-graphene into SnO$_2$ ETL further boosted the device PCE to 20.2% for device D, attributed principally to a high FF of 82%, which was close to the FF of the Shockley−Queisser efficiency limit. Furthermore, the good reproducibility for FFs (Figure S11) and the little hysteresis phenomenon from the J−V curves in both the forward- and reverse-scan direction (Figure S12) also substantiate the promise of this new ETL for PSC devices. The control experiments by adding the same ratio of NDI into SnO$_2$ (SnO$_2$-5% NDI) show a negligible effect on the PCE and FF (Table S1). The photovoltage of device D (SnO$_2$-5% G ETL) is 13 mV lower than that of device C. This could be caused by the lower conduction band of the SnO$_2$-5% G as compared to that of SnO$_2$, if considering the output voltage of PSCs principally depends on the quasi-equilibrium charge Fermi levels of the perovskite layer and the energy band offset between the ETL/perovskite and HTL/perovskite interfaces.[43−45] The inset of Figure 4e shows the steady-state output power of devices C and D in ambient conditions under continuous AM 1.5 G illumination at a constant bias. The device D showed a maximum output power of 20.2 mW cm^{-2} under 0.94 V. These results verify the good device stability of PSC devices with SnO$_2$ ETL with NDI-graphene under working conditions. The stability of these devices has been further demonstrated in the stability test, in which we measured the encapsulated ones placed in a ventilated cabinet over 300 h with 30% relative humidity at room temperature in the dark. The normalized PCE was tracked every 20 h (Figure S13). Figure 4f shows the external quantum efficiency (EQE) of PSCs with different ETLs. The EQE profiles are similar for all different devices with the maximum EQE of 85% at ~560 nm. The integrated J_{sc} from the EQE using the AM 1.5 reference spectra reaches about 22.5 mA cm^{-2}, which is close to that measured from the J−V curve. Finally, the addition of NDI-graphene produces a net gain in the overall solar-to-power conversion efficiency and a long-term stability performance, without significantly affecting the photocurrent and photovoltage.

Figure 5a compares the dark current of devices C and D. Device D shows a much retarded dark current in the low bias region (−0.5 to 1.0 V), indicating that this device possesses lower leakage current. A transition to a steep increase of the current above approximately 1.0 V reveals the highly efficient electron injection capability of solar cells based on SnO$_2$-5% G. The ideal factor (n) and series resistance (R_s) of devices were further derived from the slope and intercept of the linear fitting of the dark current according to eq 2, and the results are presented in Figure 5b.[46,47]

$$-\frac{dV}{dJ} = \frac{nK_bT}{e}(J_{sc} - J) - 1 + R_s \qquad (2)$$

Here, n is the ideal factor of devices, J_{sc} the current density, and R_s the series resistance. The ideal factor n and R_s for device D were evaluated as 1.95 and 1.51 Ω cm^2 and device C as 1.98 and 6.08 Ω cm^2. Theoretically, the smaller value of the ideal factor reflects the less carrier recombination at device interfaces.[48] After addition of NDI-graphene, the reduced 0.03 ideal factor showed that the carrier recombination was inhibited. At the meantime, the series resistance R_s of device D decreased by 4.57 Ω cm^2, and a lower R_s is necessary to eliminate charge loss at high bias voltages and to achieve a high fill factor. As a result, the lower R_s and slightly smaller ideal factor represent the high-quality device D.[49] Furthermore, the shunt resistance (R_{sh}) values of both devices were calculated from the inverse of the slope of J−V curves at 0 V, which were 1.22 and 12.50 kΩ cm^2 for devices C and D, respectively. The larger R_{sh} of device D means that the NDI-graphene doping SnO$_2$ for increasing R_{sh} of the solar cells was beneficial.[50]

We conducted the steady-state PL with the configuration of ITO/ETLs/FA$_{0.75}$MA$_{0.15}$Cs$_{0.1}$PbI$_{2.65}$Br$_{0.35}$ to illustrate charge transfer at the perovskite/ETL interface (Figure 5c). The PL spectra of ITO/SnO$_2$-5% G/FA$_{0.75}$MA$_{0.15}$Cs$_{0.1}$PbI$_{2.65}$Br$_{0.35}$ exhibited much lower intensity than those of ITO/SnO$_2$/FA$_{0.75}$MA$_{0.15}$Cs$_{0.1}$PbI$_{2.65}$Br$_{0.35}$. The stronger quenching phenomenon suggests that the SnO$_2$-5% G ETL could extract electrons from the perovskite absorber more efficiently, contributing to the increment of electrode collection. The time-resolved PL (TRPL) characteristics of SnO$_2$/FA$_{0.75}$MA$_{0.15}$Cs$_{0.1}$PbI$_{2.65}$Br$_{0.35}$ and SnO$_2$-5% G/FA$_{0.75}$MA$_{0.15}$Cs$_{0.1}$PbI$_{2.65}$Br$_{0.35}$ samples are shown in Figure 5d, which are fitted with a biexponential function (eq 3):

$$y = y_0 + A_1 \exp\left(-\frac{x}{\tau_1}\right) + A_2 \exp\left(-\frac{x}{\tau_2}\right) \qquad (3)$$

where τ_1 and τ_2 represent the bulk recombination in perovskite films and the delayed recombination of trapped charges, respectively.[51] As reported, when the delayed recombination of trapped charge that the device shows is shorter, the charge extraction ability that the transporting layer possesses is faster.[52] For the SnO$_2$-5% G/FA$_{0.75}$MA$_{0.15}$Cs$_{0.1}$PbI$_{2.65}$Br$_{0.35}$ sample, τ_1 was estimated to be 5.26 ns and τ_2 18.2 ns, while τ_1 was 4.71 ns and τ_2 24.9 ns for the SnO$_2$-only samples. Apparently, the perovskite film deposited on the SnO$_2$-5% G possesses a shorter τ_2 and also a lower ratio of τ_2/τ_1, indicating more efficient extraction and transfer of the photoinduced electrons, as compared to the film deposited on the SnO$_2$ ETL.

Figure 5e compares the Nyquist plot results for devices C and D at the same forward bias (1 V) under illumination. The resulting frequency analysis shows two semicircles in the Nyquist diagram. The arc in the high-frequency region is assigned to the charge transport process at the anode and cathode electrodes. The second arc in the intermediate-frequency region is related to the charge recombination process at the perovskite/electrode interface.[53,54] Device D shows a larger resistance arc for the charge recombination process, indicating a retarded interfacial charge recombination. Figure 5f further compares the obtained R_s for both devices as a function of bias by fitting the impedance spectra with the equivalent circuit as shown in the inset of Figure 5e. Interestingly, an Ohmic contact behavior was observed at wide bias range for

both devices, which might be attributed to highly conductive SnO_2 with NDI-graphene. Device D shows the lower R_s, suggesting efficient charge transportation in the SnO_2-5% G films. These results explain well an augmented FF of device D, which corresponds to the fitting result of the dark current above.

In conclusion, the hydrophobic carbonaceous NDI-graphene was first incorporated into SnO_2 nanocrystal film to fix octahedral $[PbI_6]^{4-}$ through forming van der Waals interaction at the perovskite/ETL interface. By using the SnO_2-5% G compact ETL, a high PCE of 20.2% with a high FF of 82% can be achieved with $FA_{0.75}MA_{0.15}Cs_{0.1}PbI_{2.65}Br_{0.35}$ perovskite, which could be ascribed to the enhancement of electron mobility, extraction ability, and the reduced carrier recombination, resulting in the augmented FF. The present work provides important guidance for further investigation in utilizing carbonaceous materials for low-temperature solution-processed planar PSCs.

Experimental Section. *Device Fabrication.* The indium-tin-oxide-coated (ITO-coated) glass was ultrasonically cleaned with detergent water, deionized water, acetone, and ethanol for 20 min, separately. The substrate was treated with UV−O_3 for 25 min. In brief, a 50 nm thick compact SnO_2, NDI-graphene/SnO_2, or SnO_2-5% NDI layer was deposited onto the ITO substrate for 30 s at 4000 rpm with a ramp of 4000 rpm s^{-1}, followed by 150 °C annealing for 30 min and 180 °C annealing for 60 min in air. The concentration of NDI aqueous solution was 1.2 mg mL^{-1}, which was the same as that of NDI-graphene. After cooling to room temperature, $FA_{0.83}MA_{0.17}PbI_{2.63}Br_{0.37}$ (PbI_2/$PbBr_2$ = 9:1, MABr/FAI = 5:1, dissolved in DMF/DMSO = 4:1) and $FA_{0.75}MA_{0.15}Cs_{0.1}PbI_{2.65}Br_{0.35}$ (PbI_2/$PbBr_2$/CsI = 9:1:1, MABr/FAI = 5:1, dissolved in DMF/DMSO = 4:1) film were prepared via a modified one-step solution process, spin-coated on top of the ETL at 5000 rpm with a ramp of 5000 rpm s^{-1} for 30 s, and chlorobenzene was dropped onto the film at the 15th second. The films were annealed in a glovebox at 120 °C for 30 min. After cooling to room temperature, a hole transporting layer was coated on the perovskite film at 3000 rpm with a ramp of 3000 rpm s^{-1} for 30 s. The hole transporting layer solution contains 70 mg of spiro-OMeTAD, 28.8 μL of TBP, and 17.5 μL of Li-TFSI/acetonitrile (520 mg mL^{-1}) per 1 mL of chlorobenzene. Finally, a gold counter electrode was deposited by thermal evaporation. The thickness of each layer was 50 nm for the SnO_2 or NDI-graphene/SnO_2 ETL, 400 nm for the perovskite layer, 180 nm for the spiro-OMeTAD layer, and 80 nm for the gold electrode. The $J−V$ measurements were performed with a metallic mask with a rectangular area of 0.1 cm^2 under AM 1.5 G 1 sun (100 mW cm^{-2}) illumination with a rate of 20 mV s^{-1} in both forward- and reverse-scan directions.

Other experimental details including device characterization and material synthesis are shown in the Supporting Information.

ASSOCIATED CONTENT

ⓢ Supporting Information

The Supporting Information is available free of charge on the ACS Publications website at DOI: 10.1021/acs.nanolett.8b00025.

    Additional experimental details and figures including AFM, SEM, UV−vis, PL, UPS, and photoelectronic properties (PDF)

AUTHOR INFORMATION

Corresponding Author
*E-mail: mingkui.wang@mail.hust.edu.cn.

ORCID Ⓘ
Yang Yang: 0000-0001-8833-7641
Mingkui Wang: 0000-0002-4516-2500

Author Contributions
X.Z., Y.S., and M.W. generated the idea. X.Z., H.L., Y.Y., and M.W. discussed the experimental plan and conducted the corresponding device fabrication and basic characterization. W.H. performed the GIWAXS measurement. L.T. performed the DFT measurement. J.L. provided the NDI-graphene material. Z.C., L.S., P.S., S.L., and Q.S. participated in the technical discussion. X.Z., Y.Y., and M.W. participated in all the data analysis and wrote the manuscript.

Notes
The authors declare no competing financial interest.

ABBREVIATIONS

ITO, indium tin oxide; ETL, electron transporting layer; PSC, perovskite solar cells; PCE, power conversion efficiency; MA, $CH_3NH_3^+$; FA, $HC(NH_2)_2^+$; FF, fill factor; DMF, dimethylformamide; DMSO, dimethylformamide; NDI, N,N'-bis-[2-(ethanoic acid sodium)]-1,4,5,8-naphthalene diimide; SEM, scanning electron microscope; NMR, nuclear magnetic resonance spectroscopy; DFT, density functional theory; ED, electron density; ELF, electron localization function; FE-TEM, field-emission transmission electron microscopy; SnO_2-1% G, SnO_2 with 1% v/v NDI-graphene; SnO_2-5% G, SnO_2 with 5% v/v NDI-graphene; SnO_2-10% G, SnO_2 with 10% v/v NDI-graphene; AFM, atomic force microscopy; RMS, root-mean-square; GIWAXS, grazing incidence wide-angle scattering spectrum; PL, photoluminescence; UPS, ultraviolet photoelectron spectroscopy; SCLC, space-charge-limited current; $J−V$, density−voltage; V_{oc}, open-circuit voltage; J_{sc}, short-circuit current density; EQE, external quantum efficiency; n, ideal factor; R_s, series resistance; TRPL, time-resolved PL

REFERENCES

(1) Yang, W.; Park, B.; Jung, E.; Jeon, N.; Kim, Y.; Lee, D.; Shin, S.; Seo, J.; Kim, E.; Noh, J.; Seok, S. *Science* **2017**, *356*, 1376−1379.

(2) Yi, C.; Luo, J.; Meloni, S.; Boziki, A.; Astani, N.; Grätzel, C.; Zakeeruddin, S.; Röthlisberger, U.; Grätzel, M. *Energy Environ. Sci.* **2016**, *9*, 656−662.

(3) Zuo, C.; Bolink, H. J.; Han, H.; Huang, J.; Cahen, D.; Ding, L. *Adv. Sci.* **2016**, *3*, 1500324.

(4) Wu, Z.; Bai, S.; Xiang, J.; Yuan, Z.; Yang, Y.; Cui, W.; Gao, X.; Liu, Z.; Jin, Y.; Sun, B. *Nanoscale* **2014**, *6*, 10505−10510.

(5) Zhou, H.; Chen, Q.; Li, G.; Luo, S.; Song, T.; Duan, H.-S.; Hong, Z.; You, J.; Liu, Y.; Yang, Y. *Science* **2014**, *345*, 542−546.

(6) Dong, H. P.; Li, Y.; Wang, S. F.; Li, W. Z.; Li, N.; Guo, X. D.; Wang, L. D. *J. Mater. Chem. A* **2015**, *3*, 9999−10004.

(7) Min, J.; Zhang, Z.-G.; Hou, Y.; Quiroz, C. O. R.; Przybilla, T.; Bronnbauer, C.; Guo, F.; Forberich, K.; Azimi, H.; Ameri, T.; Spiecker, E.; Li, Y.; Brabec, C. J. *Chem. Mater.* **2015**, *27*, 227−234.

(8) Shockley, W.; Queisser, H. *J. Appl. Phys.* **1961**, *32*, 510−519.

(9) Wu, C.-G.; Chiang, C.-H.; Tseng, Z.-L.; Nazeeruddin, M. K.; Hagfeldt, A.; Grätzel, M. *Energy Environ. Sci.* **2015**, *8*, 2725−2733.

(10) Calió, L.; Kazim, S.; Grätzel, M.; Ahmad, S. *Angew. Chem., Int. Ed.* **2016**, *55*, 14522−14545.

(11) Leblebici, S.; Leppert, L.; Li, Y.; Lillo, S.; Wickenburg, S.; Wong, E.; Lee, J.; Melli, M.; Ziegler, D.; Angell, D.; Ogletree, D.; Ashby, P.; Toma, F.; Neaton, J.; Sharp, I.; Bargioni, A. *Nat. Energy* **2016**, *1*, 16093.

(12) Oku, T.; Zushi, M.; Imanishi, Y.; Suzuki, A.; Suzuki, K. *Appl. Phys. Express* **2014**, *7*, 121601.

(13) Lee, Y.; Luo, J.; Baker, R.; Gao, P.; Grätzel, M.; Nazeeruddin, M. *Adv. Funct. Mater.* **2015**, *25*, 3925−3933.

(14) Shao, Y.; Fang, Y.; Li, T.; Wang, Q.; Dong, Q.; Deng, Y.; Yuan, Y.; Wei, H.; Wang, M.; Gruverman, A.; Shield, J.; Huang, J. *Energy Environ. Sci.* **2016**, *9*, 1752−1759.

(15) Zuo, L.; Dong, S.; Marco, N.; Hsieh, Y.; Bae, S.; Sun, P.; Yang, Y. *J. Am. Chem. Soc.* **2016**, *138*, 15710−15716.

(16) Son, D.; Lee, J.; Choi, Y.; Jang, I.; Lee, S.; Yoo, P.; Shin, H.; Ahn, N.; Choi, M.; Kim, D.; Park, N. *Nat. Energy* **2016**, *1*, 16081.

(17) Cao, D.; Stoumpos, C.; Malliakas, C.; Katz, M.; Farha, O.; Hupp, J.; Kanatzidis, M. *APL Mater.* **2014**, *2*, 091101.

(18) Chang, J.; Zhu, H.; Xiao, J.; Isikgor, F.; Lin, Z.; Hao, Y.; Zeng, K.; Xu, Q.; Ouyang, J. *J. Mater. Chem. A* **2016**, *4*, 7943−7949.

(19) Wharf, I.; Gramstad, T.; Makhija, R.; Onyszchuk, M. *Can. J. Chem.* **1976**, *54*, 3430−3438.

(20) Wu, Y.; Islam, A.; Yang, X.; Qin, C.; Liu, J.; Zhang, K.; Peng, W.; Han, L. *Energy Environ. Sci.* **2014**, *7*, 2934−2938.

(21) Yang, W.; Noh, J.; Jeon, N.; Kim, Y.; Ryu, S.; Seo, J.; Seok, S. *Science* **2015**, *348*, 1234−1237.

(22) Jeon, N.; Noh, J.; Kim, Y.; Yang, W.; Ryu, S.; Seok, S. *Nat. Mater.* **2014**, *13*, 897−903.

(23) Ahn, N.; Son, D.; Jang, I.; Kang, S.; Choi, M.; Park, N. *J. Am. Chem. Soc.* **2015**, *137*, 8696−8699.

(24) Wakamiya, A.; Endo, M.; Sasamori, T.; Tokitoh, N.; Ogomi, Y.; Hayase, S.; Murata, Y. *Chem. Lett.* **2014**, *43*, 711−713.

(25) Jo, Y.; Oh, K.; Kim, M.; Kim, K.; Lee, H.; Lee, C.; Kim, D. *Adv. Mater. Interfaces* **2016**, *3*, 1500768.

(26) Roldán-Carmona, C.; Gratia, P.; Zimmermann, I.; Grancini, G.; Gao, P.; Grätzel, M.; Nazeeruddin, M. *Energy Environ. Sci.* **2015**, *8*, 3550−3556.

(27) Somsongkul, V.; Lang, F.; Jeong, A.; Rusu, M.; Arunchaiya, M.; Dittrich, T. *Phys. Status Solidi RRL* **2014**, *8*, 763−766.

(28) Xie, J.; Huang, K.; Yu, X.; Yang, Z.; Xiao, K.; Qiang, Y.; Zhu, X.; Xu, L.; Wang, P.; Cui, C.; Yang, D. *ACS Nano* **2017**, *11*, 9176−9182.

(29) Yang, P.; Hu, Z.; Zhao, X.; Chen, D.; Lin, H.; Lai, X.; Yang, L. *ChemistrySelect* **2017**, *2*, 9433−9437.

(30) Chen, P.-Y.; Yang, S.-H. *Opt. Mater. Express* **2016**, *6*, 3651−3669.

(31) Bera, A.; Wu, K.; Sheikh, A.; Alarousu, E.; Mohammed, O. F.; Wu, T. *J. Phys. Chem. C* **2014**, *118*, 28494−28501.

(32) Zhu, Z.; Bai, Y.; Liu, X.; Chueh, C.-C.; Yang, S.; Jen, A. K.-Y. *Adv. Mater.* **2016**, *28*, 6478−6484.

(33) Ke, W.; Fang, G.; Liu, Q.; Xiong, L.; Qin, P.; Tao, H.; Wang, J.; Lei, H.; Li, B.; Wan, J.; Yang, G.; Yan, Y. *J. Am. Chem. Soc.* **2015**, *137*, 6730−6733.

(34) Zhang, L.; Zhang, Z.; He, C.; Dai, L.; Liu, J.; Wang, L. *ACS Nano* **2014**, *8*, 6663−6670.

(35) Hernandez, Y.; Nicolosi, V.; Lotya, M.; Blighe, F.; Sun, Z.; De, S.; McGovern, I.; Holland, B.; Byrne, M.; Gun'Ko, Y.; Boland, J.; Niraj, P.; Duesberg, G.; Krishnamurthy, S.; Goodhue, R.; Hutchison, J.; Scardaci, V.; Ferrari, A.; Coleman, J. *Nat. Nanotechnol.* **2008**, *3*, 563−568.

(36) Navas, J.; Coronilla, A. S.; Gallardo, J. J.; Martín, E. I.; Hernández, N. C.; Alcántara, R.; Lorenzo, C. F.; Calleja, J. M. *Phys. Chem. Chem. Phys.* **2015**, *17*, 23886−23896.

(37) Jeon, N.; Noh, J.; Yang, W.; Kim, Y.; Ryu, S.; Seo, J.; Seok, S. *Nature* **2015**, *517*, 476−480.

(38) Li, Z.; Yang, M.; Park, J.; Wei, S.; Berry, J.; Zhu, K. *Chem. Mater.* **2016**, *28*, 284−292.

(39) Li, D.; Hu, L.; Xie, Y.; Niu, G.; Liu, T.; Zhou, Y.; Gao, L.; Yang, B.; Tang, J. *ACS Photonics* **2016**, *3*, 2122−2128.

(40) Huang, W.; Huang, F.; Gann, E.; Cheng, Y.; McNeill, C. *Adv. Funct. Mater.* **2015**, *25*, 5529−5536.

(41) Lin, Y.; Shen, L.; Dai, J.; Deng, Y.; Wu, Y.; Bai, Y.; Zheng, X.; Wang, J.; Fang, Y.; Wei, H.; Ma, W.; Zeng, X. C.; Zhan, X.; Huang, J. *Adv. Mater.* **2017**, *29*, 1604545.

(42) Wang, J. T.-W.; Ball, J. M.; Barea, E. M.; Abate, A.; Webber, J. A. A.; Huang, J.; Saliba; Sero, M.; I, M.; Bisquert, J.; Snaith, H. J.; Nicholas, R. J. *Nano Lett.* **2014**, *14*, 724−730.

(43) Wang, M.; Grätzel, C.; Moon, S.; Baker, R.; Iten, N.; Zakeeruddin, S.; Grätzel, M. *Adv. Funct. Mater.* **2009**, *19*, 2163.

(44) Zuo, C.; Ding, L. *Small* **2015**, *11*, 5528−5532.

(45) Chen, W.; Xu, L.; Feng, X.; Jie, J.; He, Z. *Adv. Mater.* **2017**, *29*, 1603923.

(46) Dong, Q.; Shi, Y.; Wang, K.; Li, Y.; Wang, S.; Zhang, H.; Xing, Y.; Du, Y.; Bai, X.; Ma, T. *J. Phys. Chem. C* **2015**, *119*, 10212−10217.

(47) Hegedus, S.; Shafarman, W. *Prog. Photovoltaics* **2004**, *12*, 155−176.

(48) Liao, P.; Zhao, X.; Li, G.; Shen, Y.; Wang, M. *Nano-Micro Lett.* **2018**, *10*, 5−12.

(49) Li, H.; Tao, L.; Huang, F.; Sun, Q.; Zhao, X.; Han, J.; Shen, Y.; Wang, M. *ACS Appl. Mater. Interfaces* **2017**, *9*, 38967−38976.

(50) Min, J.; Zhang, Z.-G.; Hou, Y.; Quiroz, C. O. R.; Przybilla, T.; Bronnbauer, C.; Guo, F.; Forberich, K.; Azimi, H.; Ameri, T.; Spiecker, E.; Li, Y.; Brabec, C. J. *Chem. Mater.* **2015**, *27*, 227−234.

(51) Li, Y.; Zhao, Y.; Chen, Q.; Yang, Y.; Liu, Y.; Hong, Z.; Liu, Z.; Hsieh, Y.; Meng, L.; Li, Y.; Yang, Y. *J. Am. Chem. Soc.* **2015**, *137*, 15540−15547.

(52) Ke, W.; Zhao, D.; Xiao, C.; Wang, C.; Cimaroli, A.; Grice, C.; Yang, M.; Li, Z.; Jiang, C.; Jassim, M.; Zhu, K.; Kanatzidis, M.; Fang, G.; Yan, Y. *J. Mater. Chem. A* **2016**, *4*, 14276−14283.

(53) Juarez-Perez, E. J.; Wußler, M.; Santiago, F.; Wollny, K.; Mankel, E.; Mayer, T.; Jaegermann, W.; Sero, I. *J. Phys. Chem. Lett.* **2014**, *5*, 680−685.

(54) Li, H.; Shi, W.; Huang, W.; Yao, E.; Han, J.; Chen, Z.; Liu, S.; Shen, Y.; Wang, M.; Yang, Y. *Nano Lett.* **2017**, *17*, 2328−2335.